Innovative monolithic integrated optic SWIR SWIFTS without lens between unprotected InGaAs area image sensor and optical glass chip surface

Alain Morand, Noémie Mestre, Salma Baccar, Mohammed Irar, Grégory Grosa, Aude Bouchard, Pierre Benech, Guillermo Martin

Research Article | Vol. 33, No. 16 / 11 Aug 2025 / Optics Express 34030
Optics EXPRESS

Innovative monolithic integrated optic SWIR SWIFTS without lens between unprotected InGaAs area image sensor and optical glass chip surface

ALAIN MORAND,[1,*] NOÉMIE MESTRE,[1,2] SALMA BACCAR,[1,2] MOHAMMED IRAR,[3] GRÉGORY GROSA,[1] AUDE BOUCHARD,[1] PIERRE BENECH,[1] AND GUILLERMO MARTIN[1,2]

[1] *Univ. Grenoble Alpes, CNRS, Grenoble INP, CROMA, Grenoble 38016, France*
[2] *Univ. Grenoble Alpes, CNRS, IPAG, Grenoble 38058, France*
[3] *Univ. Grenoble Alpes, CNRS, Grenoble INP, CIME Nanotech, Grenoble 38016, France*
[*] *alain.morand@univ-grenoble-alpes.fr*

Abstract: A complete monolithic spectrometer device in the short wave infrared using integrated waveguide technology on a glass chip (i.e., without any optical lens interposer) is presented. It is based on stationary wave integrated Fourier transform spectrometer (SWIFTS) technology. The spectrometer achieves a spectral resolution of less than 300 pm for only a 2560 μm waveguide observed length and within a 7 nm repetitive spectral bandwidth due to a 60 μm sampling period. It employs nanoscale antennas to sample stationary waves within a surface-integrated waveguide, generating an under-sampled Fourier interferogram. Thanks to multi-nanowire antenna design, the system eliminates the need for bulky optical setups and it becomes compact and stable. Additionally, an optimized data reduction method is proposed to improve the spectral resolution and reduce the aliasing effect. With what we believe to be a novel approach, in a wavelength-meter configuration, a spectral resolution of 50 pm is demonstrated over a 14 nm spectral range. This initial demonstration paves the way for more complex and efficient integrated spectrometers in the future with the SWIFTS technology.

1. Introduction

Micro-spectrometers are pivotal in numerous applications, including chemistry, biomedical engineering, environmental gas monitoring, astronomy and optical metrology [1,2]. Various technologies have been explored and reviews categorizing them based on spectral resolution, compactness and the achievable spectral bandwidth have been published [3–9]. For on-board applications, reducing the footprint is crucial, especially in infrared applications requiring cooling requiring the development of compact systems.

Visible SWIFTS technology initially developed for visible light using Silicon detectors [11,12] has enabled the commercialization of spectrometers with resolutions of approximately 10pm in wide-band or sub-picometer in wavelength-meter configurations. This technology integrates an optical glass chip glued directly onto a CMOS detector (without its glass window) eliminating the need for intermediate optical setups. This optimizes camera pixel usage and enhances compactness. The technology operates by locally under-sampling the optical field of counter-propagating optical modes in a surface waveguide using Evanescent Field Scatterers (EFSs), which are metal nanowires arranged along the surface waveguide [13]. Backward and forward

#562340 https://doi.org/10.1364/OE.562340
Journal © 2025 Received 25 Mar 2025; revised 22 Jun 2025; accepted 22 Jun 2025; published 1 Aug 2025

Optics EXPRESS

fields under the EFS are radiated through the superstrate before interfering in the pixel's active zone providing intensity proportional to a sampling point of the stationary wave inside the waveguide. By associating each EFS with a pixel in a linear array, a Fourier interferogram is measured, and an inverse Fourier transform retrieves the optical source spectrum. The spectral resolution $\delta\lambda$ is primarily determined by the length L sampled given by:

$$\delta\lambda = \lambda^2/(2n_{wg}L) \tag{1}$$

with n_{wg} the effective index of the guided mode. The repetitive spectral range unaffected by spectrum aliasing is limited by the EFS period, Λ_{EFS}, expressed as:

$$\Delta\lambda = \lambda^2/(4\Lambda_{EFS}n_{wg}L). \tag{2}$$

In visible SWIFTS, one pixel by EFS is the optimal situation i.e. $\Lambda_{EFS} = \Delta x$. Thus, spectral resolution is constrained by the pixel array length and spectral bandwidth by the pixel pitch Δx, both features of the detector used. Aliasing due to the under-sampling is avoided by limiting the measurement to a spectrum of the source contained in the spectral bandwidth $\Delta\lambda$. If it is not the case, an alternative is to use band-pass filter adapted to the bandwidth where no aliasing occurs.

In the SWIR range, several SWIFTS versions have been proposed, but they require custom-built microscopy systems with at least one objective lens and then a InGaAs camera module. Unlike silicon sensors used in the visible spectral range, infrared imagers do not allow approaching the surface as closely as necessary. Various technology platforms have been used as Silicon photonic [14], Silicon Nitride [15], hybrid Silicon Nitride / Lithium Niobate [16] and thin film Lithium Niobate [17]. All of them use a single metal nanowire as EFS. However, the full system integration remains incomplete as the detector of camera module is not hybridized with the optical chip resulting in bulky setups with mechanical alignments that compromise stability. The optical transfer function of these setups can limit the optical field of view and spatial resolution of the observed zone. Shifting from visible to SWIR is further complicated by differences in detection technologies: CMOS active layers are in direct contact with the pixel surface, whereas InGaAs detectors have active layers $\approx 300\mu$m below the surface (back-illuminated), necessitating modifications to the glass optical chip and making the SWIFTS technology lose some of its appeal. Indeed, SWIR area sensors are made using an hybrid technology associating a photosensitive area in InGaAs and a CMOS signal processing circuit via electrical bumps.

In Table 1, different features of integrated spectrometers cited in this paper are shown. The sample number can be associated to the number of antennae in the SWIFTS technology, the period number of a diffracted grating as in the co-propagative SWIFTS or the asymmetric MZI used in Spatial Heterodine Spectrometers. The wavelength center is estimated to define the type of detector used CMOS in the NIR or InGaAs for example in the SWIR. Active is selected to yes if there is a temporal evolution needed via electro-optic, thermo-optic effect or the use of moveable mirror. The MEMS devices suffer from mechanical defects inducing the difficulty to ensure moving reproducibility. Thermo-optic or electro-optic effects can induce non-linear responses, time drifts complicated their monitoring. For static families, Mach Zenhder Interferometer (MZI) arrays which of their number integrated in one chip is necessarily limited to the size of each Optical Path Difference (OPD). Indeed the contra-propagative wave in a single waveguide is the best way to have the best integration associated to the longest OPD (in fact the optimized ratio length over spectral resolution) compared to dispersive grating or asymmetric MZI.

We propose different solutions to overcome these difficulties to keep the efficiency of the visible SWIFTS version when shifting to the SWIR range using a glass integrated chip as a substrate for waveguide fabrication. Ion exchange in this mature technology offers low propagation losses (close to 0.1dB/cm [18]) and minimal fiber-waveguide coupling losses, with similar mode profiles and reduced Fresnel losses through specific glue transitions. The amorphous nature of the glass wafer makes it less sensitive to external perturbations compared to Lithium Niobate thin-Film. To

Optics EXPRESS

Table 1. Characteristics of different spectrometers cited in this paper. The number of sample gives the spatial or spectral sampling elements. If a phase shift is achieved during the acquistion the device is considered active. The acronym ASn is written if *n* asymmetric Gabor loops are used. Sn for symmetric loop. The acronym Wn is written to define the number of waveguides analyzed in a spatial multiplexing case.

Spectrometer type	Number of samples	Spectral Resolution (GHz)	Bandwidth (THz)	λ_{center} (nm)	Active	On-chip detector integration	Ref
SWIFTS Gabor LNOI AS1	89	591	45	1460	Yes	No	[17]
SWIFTS Gabor LNOI AS2	89	290	45	1460	Yes	No	[17]
SWIFTS Gabor LNOI AS3	89	145	45	1460	Yes	No	[17]
3 Stage dFT	64	24.6	2.47	1550	Yes	Yes	[10]
SWIFTS Gabor LNOI S1	87	774	70	1460	Yes	No	[16]
SWIFTS Gabor SOI S1	29	500	12	1550	No	No	[14]
Co-Progative SWIFTS Ni W1	1426	2247	14	895	No	No	[15]
SWIFTS Lippman W1	2048	5.7	3.5	830	No	Yes	[11]
SWIFTS Lippman W32	32768	21.3	565	830	No	Yes	[11]
SWIFTS Lippman W1 (λ tracking)	2048	0.02	119	830	No	Yes	[12]
FTS Monopixel W1	1	3042	900	1570	Yes	No	[5]
SWIFTS Gabor Glass S1	42	37.5	0.87	1550	No	Yes	This work
SWIFTS Gabor Glass S1 (λ tracking)	42	6.2	1.75	1550	No	Yes	This work

improve the directivity of the radiated field from the EFS, radiating antenna consisting on a small grating of 5 sampling centers periodically spaced instead of a single nanowire [19] demonstrating negligible crosstalk. Unlike electro-optic solutions, we aim to use a totally passive component for the time being for easier measurement analysis. Nevertheless, the proposed component remains a building block for a more complex system. Indeed, other pixel lines of the 2D camera can be used to analyze multiple waveguides simultaneously, employing spatial multiplexing to enhance spectral resolution and/or bandwidth analyzed.

2. Design and realization

Counter-propagating waves are obtained by adding a mirror at the end of the waveguide, similar to the visible SWIFTS configuration, resulting in a Lippmann spectrometer setup. Alternatively, a straight waveguide followed by a Y-junction can equally split the optical path and superimpose the waves using a loop, forming a Gabor spectrometer configuration [16]. The Lippmann setup ensures a zero optical path difference (zOPD) at the mirror but can suffer from uncoupled reflected signals that pollute the visualization and unbalance wave amplitudes. As a result, only half of the interferogram is usable, making it more difficult to study phase shifts linked to fringe asymmetry. This issue is significantly reduced in the Gabor configuration. However, the zOPD position may deviate from the expected location due to minor optical path variations generated during the fabrication steps. Despite this, the interferogram remains stable due to the homogeneous optical features of the chip across the wafer. This configuration, illustrated in the third-level lithography masks in Fig. 1, employs Euler bends for transitions between straight and bend waveguides, with a loop bend radius of 1500μm slightly higher than the smallest bend usable in this technology close to 1000μm.

These optical structures were fabricated on a glass substrate with a diameter of 6cm and a thickness of 1.5mm. They are surface optical guides created through Ag^+/Na^+ ion exchange using an initial aluminum mask. Metallic marks are retained to align a secondary Cr/Au mask, enhancing visibility for electron-beam alignment. A $36 \times 36 mm^2$ section of the chip is extracted by dicing, with two faces simultaneously polished for fiber-waveguide coupling. The alignment marks are then used in electron-beam lithography to fabricate Ti/Au antennas on the surface waveguides via a lift-off process. Each EFS consists of an antenna with 5 metal nanowires (50nm thick $\times$100nm long $\times$100μm width). This nanowire grating acts as an equivalent Bragg grating

Optics EXPRESS

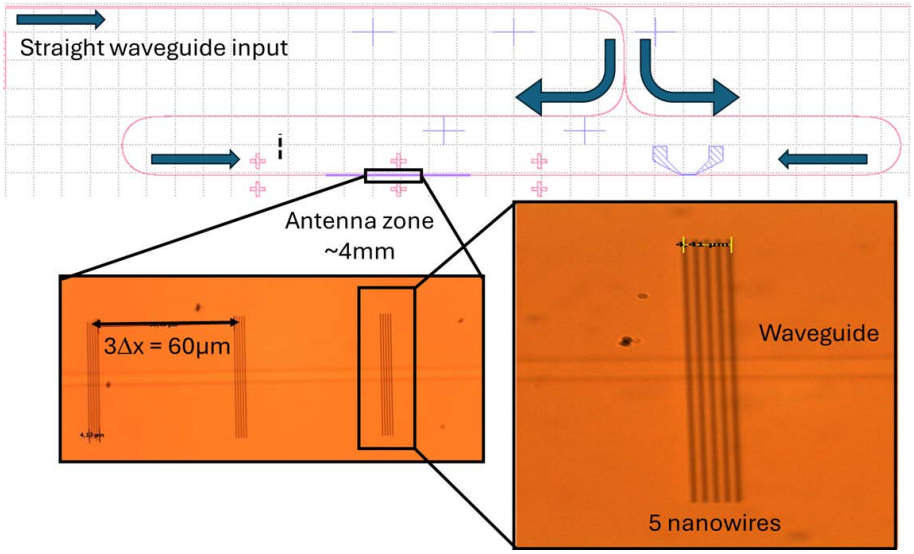

Fig. 1. On the top, layout sketch of the Gabor loop design. Bottom pictures show the periodically spaced antenna, each of them constituted of small grating containing 5 nanowires composed of a bilayer Ti/Au, across the waveguide.

converting the evanescent field into vertical radiation with a smaller numerical aperture than a single nanowire. As shown in Fig. 2, the angular divergence is reduced with the increasing number of nanowires forming the grating. In order to ensure constructive interaction between single nanowire radiation in a quasi-vertical direction, the grating period must be $\Lambda_n = \lambda_{ref}/n_{wg}$ for the spectral bandwidth containing the reference wavelength λ_{ref} = 1550nm. Starting from the 4-nanowire grating, only 6 pixels are illuminated. The pitch is then too large to observe a noticeable intensity variation from higher number of nanowires.

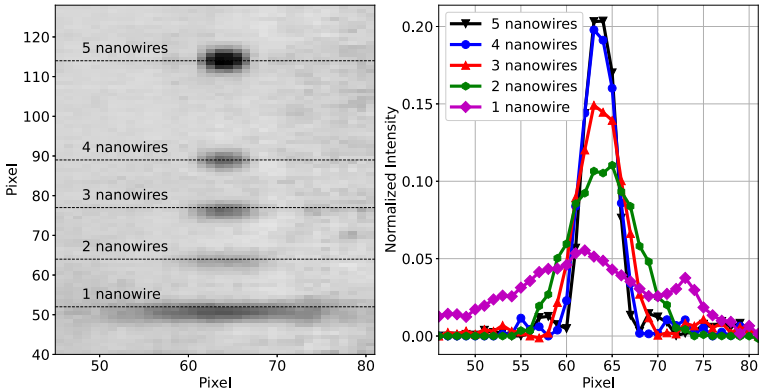

Fig. 2. On the left, 2D radiated view with decreasing number of nanowires per antenna (from top to bottom 5, 4, 3, 2 and 1). The horizontal black lines are the different waveguide axis for each case. And on the right, horizontal intensity profile as extracted from the antenna, depending on the number of nanowires.

The period of the antennas' pattern Λ_{EFS} is set to 3 pixels, $3\Delta x = 60\mu$m to avoid crosstalk between antennas on the camera. To analyze the chip response, two tunable sources are used: one from SANTEC as a calibration (reference) and another from TUNICS as an unknown wavelength

Optics EXPRESS

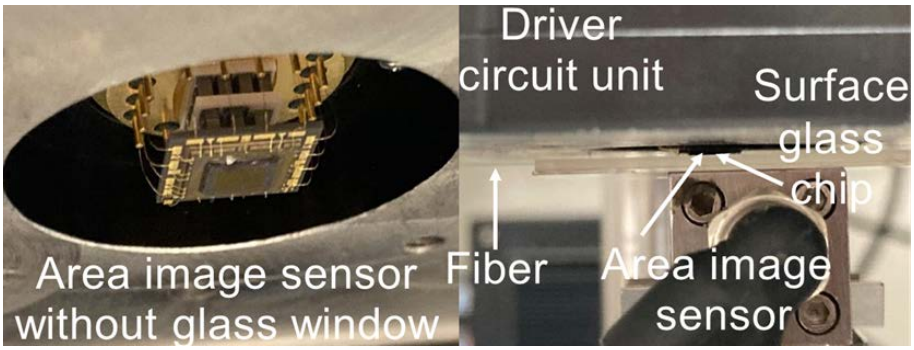

Fig. 3. On the left, area image sensor without glass window. On the right glass chip set close to the detector surface.

(guess). Both sources are linearly polarized and injected in a polarization-maintaining fiber. An attenuator can be employed to prevent detector saturation by controlling the signal level. The signal is injected into the chip in TE polarization to optimize antenna radiation efficiency [13]. A Hamamatsu $G12242$ 128×128 pixel area image sensor with 20μm pitch is used. This sensor is connected to a $C11512$ driver circuit unit which is linked to a computer via a Camera Link frame grabber. The uncapped version of the area image sensor allows direct contact between the InP layer and the glass chip surface, as illustrated in Fig. 3. The camera's image capture is synchronized using a clock signal from the laser connected to the camera's trigger input. The mechanical setup controls the camera's position in three directions, while a micro-positioner adjusts the angle in the chip's plane to align the pixel array with the waveguide propagation axis.

3. Characterization

The initial step involves creating a calibration table by recording the under-sampled Fourier interferogram frame by frame for each wavelength scanned with the SANTEC source. The image is processed to retain only the 1D profile of the interferogram along the waveguide direction, covering the whole 128 pixels length, for each case. This allows for the definition of a spatial pattern which visualizes the evolution of the interferogram along the pixels (horizontal axis) as a function of wavelength (vertical axis), as depicted in Fig. 4. A zOPD is observed around pixel 110, where maximum intensity is noted for all wavelengths. Since the signal is monochromatic, the intensity evolution along the waveguide follows a cosine function with a period that varies with wavelength. This function is defined by:

$$I_0[1 + \cos(4\pi n_{wg}\sigma(x - x_0))] \text{ with } \sigma = 1/\lambda \tag{3}$$

x_0 a potential shift or relative optical path difference which is theoretically set to 0 on the mask. The antenna array are aligned along the straight waveguide part in order to have an antenna at $x = 0$. The intensity of the backward and forward optical beams are assuming identical. This function is under-sampled by the antennas distributed along the waveguide and the intensity evolution is also a cosine function resulting from the under-sampling of the Eq. (3). On the right of the Fig. 4, it is shown the same evolution in the spectral domain after applying an inverse fast-Fourier transform (FFT) along the waveguide axis. A zoom of this figure is also shown in the inset window.

The specific pattern in the left figure repeated along the vertical axis and defined by $\Delta\lambda$ corresponds to a single band in the right figure. The under-sampling aliased frequency σ_p in pixel^{-1} evolves linearly within the first aliasing band from 0 to 0.17 pixel^{-1}. Indeed, the pattern period $\Lambda_{EFS} = 3\Delta x$ is three times the pixel pitch Δx of the camera used here, allowing

Optics EXPRESS

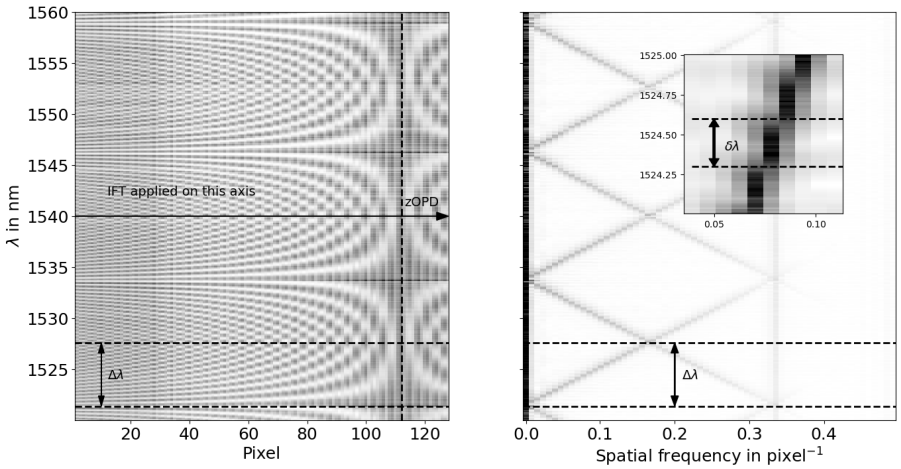

Fig. 4. On the left, the evolution of the intensity (interferogram) as a function of the pixel in the horizontal axis and function as the wavelength in the vertical axis. On the right, an inverse Fourier Transform has been applied along the pixel axis to retrieve the optical spectrum source which is the spectral density as a function of the frequency σ_p in pixel^{-1}. In the inset window, a zoom on the retrieved peak is shown, to get an idea of spectral resolution.

visualization of nearly all the radiation from an antenna. The maximum frequency observable is then 0.5/3 pixel^{-1}. To link the wavelength source λ to the frequency σ_p in pixel $^{-1}$ given by the SWIFTS, the following equation must be used:

$$S(2n_{wg}\sigma - m\sigma_e/\Delta x) = \sigma_p/\Delta x \iff \sigma = (m\sigma_e + S\sigma_p)/(2n_{wg}\Delta x S) \tag{4}$$

with $\sigma_e = 1/3$ pixel^{-1}, σ_p representing the position of the maximum intensity in pixel^{-1}, m the aliasing order and $S = \pm 1$ must be chosen following the aliasing window analyzed. This equation is used as a fit as shown in Fig. 5, yielding $m = 120$ and $n_{wg} = 1.521$ with $S = -1$ (case where λ increases with σ_p). The frequency sampling step constrained by the length of the analyzed interferogram is defined as $\delta\lambda = 308$pm with $L = 128\Delta x$ and $\lambda = 1550$nm.

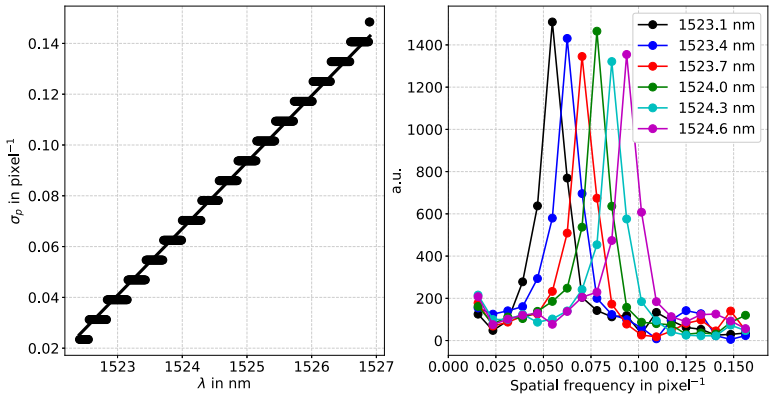

Fig. 5. On the left, σ_p along λ and on the right few spectrums from unknown wavelengths.

Additionally, a different folding occurs every $\Delta\lambda = 6.6$nm. From the same equation, the bounds of the first band range from 1521.0nm to 1527.6nm. To assess the efficiency of the SWIFTS to detect an unknown wavelength, measurements were conducted using the TUNICs

Optics EXPRESS

tunable laser. Various inverse Fourier transforms were performed with different wavelength steps, successfully retrieving the minimum wavelength step needed to separate the peak maxima. The contrast remained high, close to 11dB. Fitting the peak with a Lorentzian function confirmed a spectral resolution of approximately 280pm close to $\delta\lambda$ given previously.

An effective method to analyze cross-talk between successive antennas involves applying the Fourier transform along the vertical axis of the left Fig. 4, where the evolution follows the same cosine function of the Eq. (3). The result is shown in Fig. 6. Along the vertical axis, the frequency of the cosine function is $2n_{wg}x$ with x representing the antenna's position from the zOPD. In the Fourier domain, each pixel produces a specific peak at a frequency proportional to x. The peak's width along this axis depends on the scanned wavelength range, while its width along the pixel axis indicates the radiated field zone of an antenna. Along this axis, the radiated intensity spreading of each antenna is mainly over 3 pixels. The intensity of the neighboring antennas can induce cross-talk if intensities of two antenna are superposed on the same pixel which can degrade the interferogram. As shown on the right part of Fig. 6, this superposition remains low and confirms a low cross-talk. A balance must be found between minimizing this cross-talk and maximizing the spectrum from 0 to 0.5 pixel^{-1} instead of 0 to 0.5/3 pixel^{-1}.

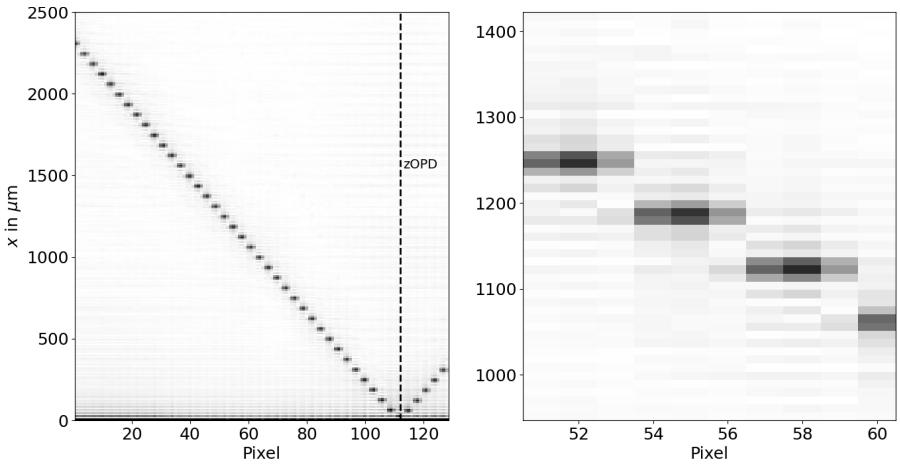

Fig. 6. At the left, x gives the position of antenna from zOPD as a function of the pixel of the detector. The dashed line is set at zOPD. At the right, a zoom over three chosen antennas. The horizontal separation between two successive maxima is $3\Delta x = 60\mu$m.

4. Wavelength-meter characterization

A believed to be novel calibration process is proposed to more accurately track the evolution of an unknown wavelength. This method involves comparing the unknown spectrum obtained from the SWIFTS $F_{\lambda_{sought}}(\sigma_p)$ with all the spectra from the calibration scan $F_{\lambda_{cal}}(\sigma_p)$. Before realizing this operation, the part of the signal at the null frequency is canceled (which is equivalent to subtract the mean value of each interferogram) and all the spectra are normalized in intensity. The advantage of this approach is the potential to increase the spectral resolution although it is limited to measuring monochromatic optical sources, effectively turning the spectrometer into a wavelength-meter. The wavelength accuracy depends on the 10pm wavelength scan step and the efficiency of SWIFTS. For each calibration wavelength λ_{cal}, a correlation operation is performed $C(\lambda_{cal}) = \mathbb{R}\int F_{\lambda_{unknown}}(\sigma_p).F^*_{\lambda_{cal}}(\sigma_p)d\sigma_p$. This function reaches its maximum when the two spectra are closely matched as a correlation function. In Fig. 7, various wavelengths from the TUNICs monochromatic sources are analyzed. In each case, the function $C(\lambda_{cal})$ is

Optics EXPRESS

displayed. Normally, for each aliasing bandwidth without monochromatic dispersion, an aliasing peak with an amplitude of 1 must appear. In theory, an antenna is set at the zOPD where $x = 0$.

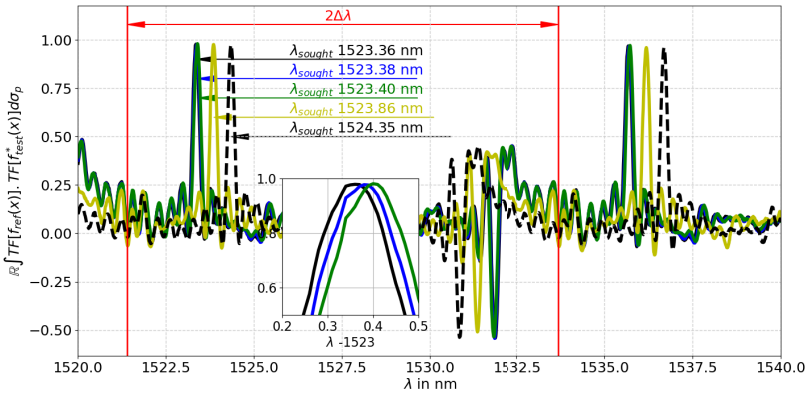

Fig. 7. Evolution of the function $C(\lambda)$ for different unknown wavelengths. The curves corresponding to the wavelength close to 1523.4nm are shown in the inset window over a smaller wavelength range (1523.36, 1523.38 and 1523.40nm).

But, in Fig. 7, the sign of the peak changes alternatively allowing us to discriminate the two peaks of two successive aliasing bandwidths. This appears if the stationary waves in the waveguide is shifted with $x_0 \neq 0$. Consequently, the optical source wavelength can be analyzed over the double SWIFTS bandwidth $2\Delta\lambda$. To demonstrate this a numerical simulation has been made and the interferogram along x is firstly sampled with the same spatial step in which an Inverse Fourier transform is applied to recover the spectrum. The same scan in wavelength is made to calculate the function $C(\lambda)$. In Fig. 8, several evolutions are depicted as a function of the spatial shift x_0. For a null OPD ($x_0 = 0$nm), the amplitudes of all peaks in each band are close to 1. As the phase shift increases, the amplitude of the second peak decreases until to attain negative values, whereas the amplitude of the first peak remains close to 1. By comparing the negative amplitude to the measured negative peak, the OPD can be determined at $x_0 = 85$nm. For further increases, the peak amplitude can reach a minimum value of -1 before increasing again. This evolution is periodic, as illustrated in the Fig. 9, and can be accurately described by a cosine function $f(x_0)$ that fits the simulated amplitude data precisely. It clearly demonstrates the phase shifting effect on the peak amplitude. This phase shifting not expected initially due to asymmetrical effect on the loop after the fabrication process can be seen as a defect but becomes here essential to increase the wavelength-meter bandwidth. Finally, the peak's FWHM is close to $\delta\lambda$, the theoretical spectral resolution. However, the peak's wavelength maximum position can be measured with greater accuracy thanks by the wavelength scan used for the calibration.

A comparison of the reconstructed wavelength and the reference wavelength, over the $2\Delta\lambda$ bandwidth, is depicted in the Fig. 10. It is shown that the wavelength difference remains at most between ±50pm. This demonstrates the capability to monitor the wavelength evolution of a monochromatic optical source with a spectral resolution 3 times higher than in the classical SWIFTS case just by using this correlation function.

Optics EXPRESS

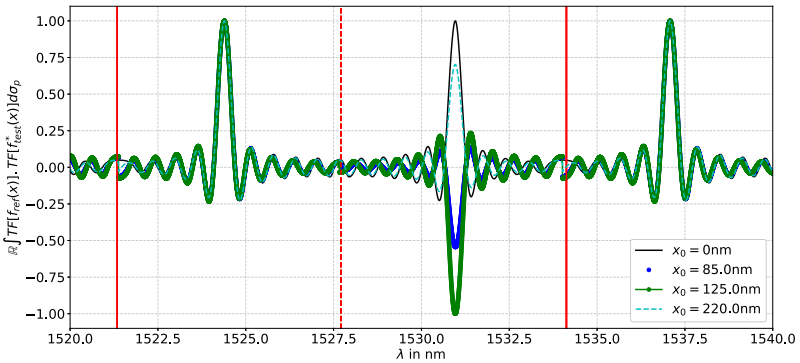

Fig. 8. Simulated evolution of $C(\lambda)$ for several specific shifts i.e. $x_0 = 0$, 85, 125 and 220nm.

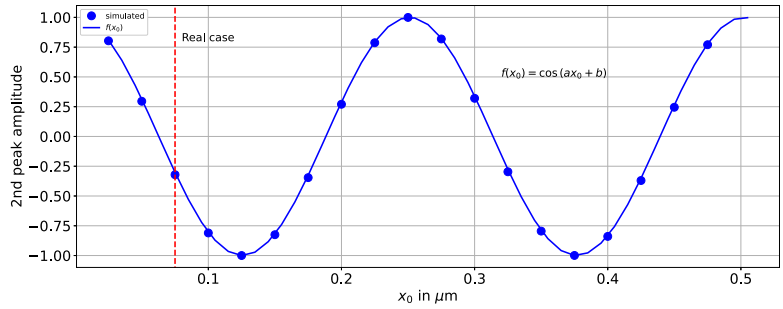

Fig. 9. Simulated amplitude of the second peak as a function of the OPD x_0, fitted by a cosine function.

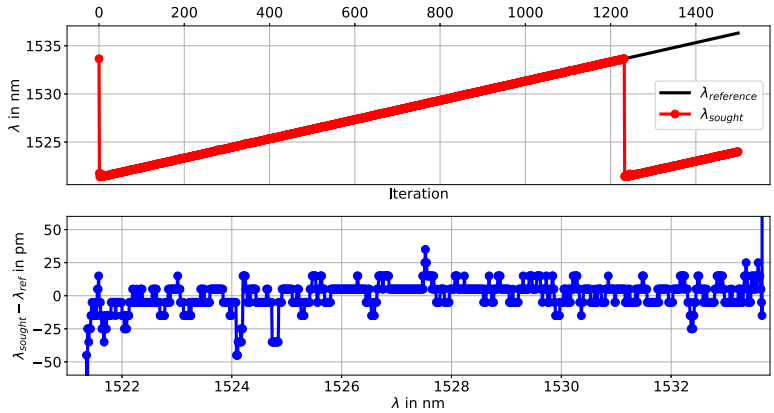

Fig. 10. On the top, evolution of unknown scan wavelength sought by the method with circle marks. The black line is the real wavelength evolution. On the bottom, the error between the sought wavelength and the reference wavelength.

Optics EXPRESS

5. Discussion

The realization of a complete monolithic SWIFTS in the SWIR has been demonstrated. In particular, the objective lens used in [17] for example is here completely suppressed. The pixel array is positioned close to the surface waveguide to directly collect the flux radiated by a pattern of antennas as an image on the sampled stationary wave. The antenna design ensures that the radiated signal in the superstrate is sufficiently directive to illuminate a maximum of 3 pixels along the propagation axis, despite the thickness of the detector's InP layer to cross. These features are crucial for achieving a SWIFTS without the need for bulky optical setups, resulting in a compact and stable device. With approximately 40 antennas, a spectral resolution of 300pm is achieved over a spectral bandwidth of nearly 7nm. This promising initial stage allows for the consideration of a more complex device utilizing spatial division multiplexing [20]. By incorporating few splitting steps in the loop within glass integrated optics, it will be possible to divide each path into few parallel waveguides. These waveguides can then be analyzed using the same InGaAs area image sensor. Indeed, the transverse diffraction can be captured using less than 8 pixels. With this last value, at least 16 waveguides can be observed along the y-axis with the same detector. Depending on the chosen zOPD gap for each waveguide, different enhancements can be achieved: each waveguide can analyze different parts of the interferogram increasing the spectral resolution by a factor 16. Or each waveguide can analyze different sampling points on the same interferogram length, increasing the spectral bandwidth by the same factor. This improvement can be generalized by a figure of merit defined by the ratio $\Delta\lambda/\delta\lambda$ i.e. the bandwidth available over the spectral resolution. This factor is proportional to the pixel number available on the detector. In this paper, only 42 antennas are used distributed over 8×128 pixels surface. If higher vertical cross-talk is accepted between each straight waveguide to reduce 8 pixels to 4 pixels, 32 waveguides each under-sampled by 42 antennas can be used which corresponds to 32×128 pixels surface of the 128×128 pixels available.

Finally, position errors can occur during the creation of the gold intermediate layer between the waveguide fabrication and antenna fabrication. In this case, classical optical lithography equipment is used to align the new mask with the waveguide already fabricated in the glass chip. Even with optimized cross marks, the position error can be as high as 1μm in the most pessimistic scenario. The antenna length defined at 100μm cancels this effect in the transverse direction of the waveguide, ensuring complete interaction of the optical mode with the antenna. However, an offset applied to all the antennas can appear in the waveguide propagation axis, potentially causing the zOPD to not be in the middle of its antenna but shifted to x_0. This relative path difference is not guaranteed to be consistent across different fabrications. Therefore, future developments should include a technique to control this relative path difference after chip fabrication and maintain it irreversibly. Over several months of different measurement runs, the chip has consistently produced high contrasted fringes. However, as long as the detector is freely positioned over the glass chip, a thorough investigation of the chip's stability is challenging. For each measurement run, the measurement bench is reassembled and the position of the pixels over the antenna can vary due to manual mechanical positioning. The next demonstrator will consist on an chip optically glued to the detector to investigate its reproducibility in the short and longer term, with a view to building a spectrometer.

Funding. Agence Nationale de la Recherche Labex FOCUS (ANR-11-LABX-0013); Région Auvergne-Rhône-Alpes grant "Pack Ambition Recherche 2021–Project (HIRESPECT (21.019042.01)).

Acknowledgment. We would like to thank Teemphotonics for fabricating the optical chip on glass, the PTA for fabricating the antennas and CIME for providing the Disco sawing equipment to cut the chip.

Disclosures. The authors declare no conflicts of interest

Data availability. Data underlying the results presented in this paper are not publicly available at this time but may be obtained from the authors upon reasonable request.

Optics EXPRESS

References

1. A. Li, C. Yao, J. Xia, *et al.*, "Advances in cost-effective integrated spectrometers," Light: Sci. Appl. **11**(1), 174 (2022).
2. J.-P. Bibring, V. Hamm, C. Pilorget, *et al.*, "The MicrOmega Investigation Onboard ExoMars," Astrobiology **17**(6-7), 621–626 (2017).
3. C. M. Coppola, M. De Carlo, F. De Leonardis, *et al.*, "i-PHAOS: An Overview with an Open-Source Collaborative Database on Miniaturized Integrated Spectrometers," MDPI Sensors **24**(20), 6715 (2024).
4. H. Yao, M. Wang, Y. Sun, *et al.*, "On-Chip Fourier Transform Spectrometer on Thin Film Lithium Niobate," J. Lightwave Technol. **42**(19), 6850–6856 (2024).
5. M. J. Grotevent, S. Yakunin, D. Bachmann, *et al.*, "Integrated photodetectors for compact Fourier-transform waveguide spectrometers," Nat. Photonics **17**(1), 59–64 (2023).
6. A. Li and Y. Fainman, "On-chip spectrometers using stratified waveguide filters," Nat. Commun. **12**(1), 2704 (2021).
7. L. Zhang, J. Chen, C. Ma, *et al.*, "Research Progress on On-Chip Fourier Transform Spectrometer," Laser Photonics Rev. **15**(9), 2100016 (2021).
8. Z. Yang, T. Albrow-Owen, T. Hasan, *et al.*, "Miniaturization of optical spectrometers," Science **371**(6528), eabe0722 (2021).
9. S. N. Zheng, J. Zou, H. Cai, *et al.*, "Microring resonator-assisted Fourier transform spectrometer with enhanced resolution and large bandwidth in single chip solution," Nat. Commun. **10**(1), 2349 (2019).
10. D. M. Kita, B. Miranda, D. Favela, *et al.*, "High-performance and scalable on-chip digital Fourier transform spectroscopy," Nat. Commun. **9**(1), 4405 (2018).
11. C. Bonneville, F. Thomas, M. de Mengin Poirier, *et al.*, "SWIFTS: a groundbreaking integrated technology for high-performance spectroscopy and optical sensors," Proc. SPIE **8616**, 86160M (2013).
12. C. Duchemin, T. Fabrice, M. Bruno, *et al.*, "Development of an integrated sub-picometric SWIFTS-based wavelength meter," Proc. SPIE **10110**, 1011016 (2017).
13. L. Arnaud, A. Bruyant, M. Renault, *et al.*, "Waveguide-coupled nanowire as an optical antenna," J. Opt. Soc. Am. A **30**(11), 2347–2355 (2013).
14. E. Le Coarer, S. Blaize, P. Benech, *et al.*, "Wavelength-scale stationary-wave integrated Fourier-transform spectrometry," Nat. Photonics **1**(8), 473–478 (2007).
15. X. Nie, E. Ryckeboer, G. Roelkens, *et al.*, "CMOS-compatible broadband co-propagative stationary Fourier transform spectrometer integrated on a silicon nitride photonics platform," Opt. Express **25**(8), A409–A418 (2017).
16. D. Pohl, M.-R. Escalé, M. Madi, *et al.*, "An integrated broadband spectrometer on thin-film lithium niobate," Nat. Photonics **14**(1), 24–29 (2020).
17. G. Finco, G. Li, D. Pohl, *et al.*, "Monolithic thin-film lithium niobate broadband spectrometer with one nanometre resolution," Nat. Commun. **15**(1), 2330 (2024).
18. ioNext, "Teemphotonics. PIC Optical Waveguides for Si-Pho, Integration & Sensors," https://www.teemphotonics.com/integrated-photonics/platform/
19. A. Morand, I. Heras, G. Ulliac, *et al.*, "Improving the vertical radiation pattern issued from multiple nano-groove scattering centers acting as an antenna for future integrated optics Fourier transform spectrometers in the near IR.," Opt. Lett. **44**(3), 542–545 (2019).
20. G. Martin, A. Morand, M. Bonduelle, *et al.*, "Nanoscale Sampling of Optical Signals: Application to High-Resolution Spectroscopy. In Ultrafast Laser Nanostructuring: The Pursuit of Extreme Scales," Cham: Springer International Publishing, 1019–1051 (2023).

90.114.4.243 2025-08-01 13:49:46